Catalysis Letters (2018) 148:1990–2000
https://doi.org/10.1007/s10562-018-2413-5

Ultrathin Hexagonal SnS_2 Nanosheets Coupled with Tetragonal $CuInS_2$ Nanosheets as 2D/2D Heterojunction Photocatalysts Toward High Visible-Light Photocatalytic Activity and Stability

Kai Zhang[1] · Yunhai Zhang[2] · WanJu Zhang[1]

Received: 4 March 2018 / Accepted: 14 May 2018 / Published online: 19 May 2018

Abstract

A kind of 2D/2D heterojunction photocatalysts was constructed by a facile in situ hydrothermal method that a tetragonal $CuInS_2$ nanosheets was horizontal loaded in ultrathin hexagonal SnS_2 nanosheets. Contrasted to pure $CuInS_2$ and SnS_2 nanosheets, the $CuInS_2/SnS_2$ nano-heterojunctions revealed a noteworthy improvement photocatalytic activity under visible light irradiation for the degradation of organic dyes, which should be attributed to the narrowest band gap and the efficient charge separation and transfer improving the contact region in heterojunction interface. Especially, with 0.5 wt% addition of $CuInS_2$, the heterojunction nanosheets shows a supreme visible-light photocatalytic activity and a superb degradation efficiency which reached 99% in 60 min with the solution of methyl orange. Moreover, $CuInS_2/SnS_2$ nano-heterojunctions deliver excellent reusability in five degradation–regeneration cycles. The results indicated that $CuInS_2/SnS_2$ has a promising prospect in organic pollutant treatment due to high efficiency and excellent stability.

Graphical Abstract

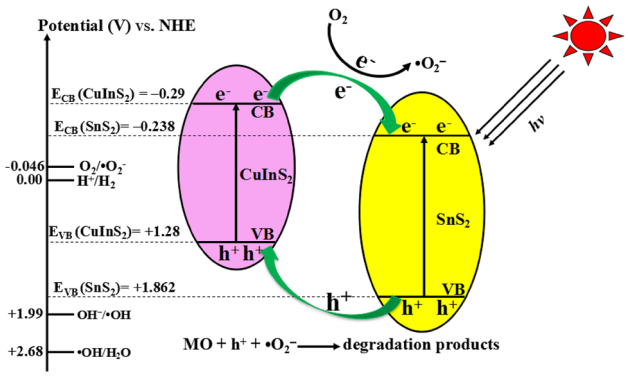

Keywords $CuInS_2/SnS_2$ · Heterojunction · In situ hydrothermal method · Visible-light photocatalysis

1 Introduction

A new wave of research activities, the efficient utilization of solar energy, has stimulated by the ever-increasing global demand for energy. Visible-light-driven semiconductor photocatalysts, a promising prospective application in the treatment of environmental pollutants in water, have created widespread interest in the scientific and technology communities [1–5]. However, solar energy conversion efficiency

✉ Yunhai Zhang
wszhyhai@foxmail.com

✉ WanJu Zhang
28813470@qq.com

Extended author information available on the last page of the article

still requires much improvement, although various strategies including bandgap engineering, crystal phase control, and microstructure construction have been employed [6, 7]. Recently, developing heterostructured materials by carefully selecting and coupling two different semiconductors has yielded novel photocatalysts with high activity [8–11].

Metal sulfides are considered promising materials for coupling with other semiconductors, due to their relatively narrow band gap. Among them, tin sulfide (SnS_2) has been attracting increasing attention for its cheap, abundant, and its low band gap (1.91–2.35 eV) as well as it can be designed as an environmental friendly visible-light photocatalyst [12–15]. However, reports showed that its photodegradation performance should be improved [14, 15]. In contrast with single semiconductor, the photocatalysts performance of the two different semiconductors composite can be successful and higher improved, which owns to the narrowest band gap and the efficient charge separation and transfer improving the contact region in heterojunction interface [16–18]. For example, SnS_2/BiOBr heterojunction nanoplates showed higher photocatalytic activity than BiOBr and SnS_2 for the degradation of rhodamine B under visible light irradiation [18]. Recently, Gao et al. achievement illustrated that the photocatalytic activity of SnS_2-based heterojunction could be obviously enhanced by way of extending the photoresponding range and increasing the charge separation efficiency [19]. Besides, Zhang et al. demonstrated that it is the RhB photodegradation apparent rate constant that under visible light is higher than that of pure g-C_3N_4 and SnS_2 nanosheets by a factor of 4 and 8, respectively [20].

The remarkable properties of narrow band gap, high stability, and strong visible-light absorption made ternary chalcogenide compounds gained tremendous attraction, and a notable candidate for the application of photocatalyst in recent years [21]. Taking Copper indium disulfide ($CuInS_2$) for example, it is an universal ternary chalcogenide semiconductor that exhibits an excellent photocatalytic property [22–24]. However, the small specific surface area and fast electron–hole recombination have brought a huge obstacle to single $CuInS_2$ semiconductors for the application of photocatalyst. Besides, the truth that subdued photocatalytic activity would incredible decrease its photocatalytic efficiency during recycling process. Moreover, it can be observed that, among those SnS_2 and copper indium disulfide ($CuInS_2$), the energy levels of the valence band (VB) and conduction band (CB) can match well between the two, which plays a synergistic effect on and benefits to the transmission of photoinduced charge carriers. Therefore, it can be theoretically find out that the $CuInS_2$/SnS_2 heterostructure composites can exhibit excellent photocatalytic activity to remove organic pollutant under visible light.

Herein, a 2D/2D heterojunction photocatalysts was constructed by a facile and simple one-step in situ hydrothermal method, through coupling the tetragonal $CuInS_2$ nanosheets with ultrathin hexagonal SnS_2 nanosheets. As such, the as-fabricated $CuInS_2$/SnS_2 heterojunction nanosheets exhibit significant enhancement on the photocatalytic activities for the degradation of organic dyes under visible light irradiation as compared to pure $CuInS_2$ and SnS_2 nanosheets. The morphology, structure, optical and electrochemical properties were characterized, and the photocatalytic activity of $CuInS_2$/SnS_2 heterojunctions was tested by photodegrading methyl orange under visible-light irradiation, and the reusability of $CuInS_2$/SnS_2 was evaluated by five consecutive photocatalytic runs. The relationship between its structure and performance, and the possible photocatalytic mechanism were also proposed.

2 Experimental

2.1 Materials and Chemicals

Tin(IV) chloride pentahydrate ($SnCl_4{\cdot}5H_2O$) was purchased from Shanghai Fengxian Chemistry Co., Ltd. (Shanghai, China). Thioacetamide (TAA) and cuprous chloride (CuCl) were attained from Tianjin Chemical Reagent Plant (Tianjin, China). Indium chloride ($InCl_3{\cdot}4H_2O$) and methyl orange (MO) were received from Aladdin Chemistry Co. Ltd. (Shanghai, China). Anhydrous ethanol, sodium sulfate (Na_2SO_4) and iso-propyl alcohol (IPA) were obtained from Shantou Xilong Chemical Co., Ltd. (Shantou, China). p-Benzoquinone (BQ) was supplied by Shanghai Crystal Pure Reagent Co., Ltd. (Shanghai, China). Triethanolamine (TEOA) was acquired from Shanghai Chemical Reagent Co., Ltd. (Shanghai, China). All chemicals and solvents were of analytical grade and used without further purifcation.

2.2 Preparation of $CuInS_2$/SnS_2 Nano-heterojunction

First, the SnS_2 nanosheets were synthesized by a hydrothermal method. Briefly, 0.02 mmol of $SnCl_4{\cdot}5H_2O$ and 0.04 mol TAA were added in 40 mL of deionized water. After stirring for 30 min, the above mixture was transferred into a Teflon-lined stainless steel autoclave with a capacity of 50 mL. The autoclave was sealed and heated at heated at 180 °C for 20 h and then was naturally cooled to room temperature. The precipitate filtered and washed with distilled water and ethanol for several times, and then dried in a vacuum oven at 100 °C for 5 h.

$CuInS_2$/SnS_2 nano-heterojunction was fabricated. First, 0.02 mol of $SnCl_4{\cdot}5H_2O$, 0.04 mol TAA were added in 40 mL of deionized water with magnetic stirring marked as solution (A) Then a certain amount $CuInS_2$ (Cu:In:S = 1:1:2) were added in 20 mL of deionized water under magnetic

stirring marked as solution (B) Finally, adding the solution B to the solution A under magnetic stirring drop by drop. After stirring for 30 min, the above mixture transferred into a Teflon-lined stainless steel autoclave with a capacity of 100 mL. The autoclave was sealed and heated at heated at 180 °C for 20 h and then was naturally cooled to room temperature. After that the product was washed with deionized water and ethanol several times, and then was obtained in a vacuum oven at 100 °C for 5 h. Samples mass ratio of $CuInS_2$ to SnS_2 were denoted as $CuInS_2/SnS_2$ (0.1%), $CuInS_2/SnS_2$ (0.5%), $CuInS_2/SnS_2$ (1%), $CuInS_2/SnS_2$ (3%) and $CuInS_2/SnS_2$ (5%), respectively.

2.3 Characterization Methods

Morphologies of $CuInS_2$, SnS_2 and $CuInS_2/SnS_2$ nano-heterojunction were examined by scanning electron microscopy (SEM, KYKY-EM3900M) and transmission electron microscope (TEM, JEM-2010F) and high-resolution transmission electron microscope (HRTEM, JEM-2010F). The crystal phase of the samples was analyzed by X-ray diffraction (XRD). BET surface areas and pore structures were analyzed using a GEMINI VII 2390 surface area and porosity analyzer (Micromeritics, USA). The reflectance spectra of the samples were obtained from a U-3900H scan UV–Vis spectrophotometer (Hitachi, Japan). The photoluminescence (PL) spectra were measured using F-7000 fluorescence spectrophotometer (Hitachi, Japan) with an excitation wavelength of 325 nm, scanning speed of 1200 nm min^{-1}, and the photomultipliers voltage of 700 V.

2.4 Electrochemical Measurement

The photocurrent of pure $CuInS_2$, SnS_2 and 0.5% $CuInS_2/SnS_2$ nano-heterojunction were determined by using a Chenhua CHI660C Electrochemical Workstation (Shanghai, China) with a standard three-electrode cell. A standard three-electrode system was composed of $CuInS_2$, SnS_2 or $CuInS_2/SnS_2$ film fabricated on FTO conductive glass (an effective area of 1 cm^2) as working electrode, KCl-saturated calomel electrode (SCE) as reference electrode, platinum plate as counter electrode, and 0.5 mol L^{-1} Na_2SO_4 as supporting electrolyte. The applied voltage was 0 V for the FTO working electrode. A 300 W xenon lamp (PLS-SXE300, Beijing Trusttech Co., Ltd. China) with a 400 nm cut off filter (400 nm $< \lambda <$ 780 nm) was used as the source of visible light.

The flat band potentials of pure $CuInS_2$, SnS_2 and 0.5% $CuInS_2/SnS_2$ nano-heterojunction were determined by Mott–Schottky plots using the same standard three-electrode system as the photocurrent test, and the applied potential ranges between − 1 and 1 V with the scan frequency of 10 kHz.

Electrochemical impedance spectroscopy (EIS) was measured as the same standard three-electrode system and electrochemical workstation as Mott–schottky test, but the electrolyte solution is the mixture of 0.5 mol L^{-1} Na_2SO_4, 2.5 mmol L^{-1} potassium hexacyanoferrate(III) ($K_3[Fe(CN)_6]$), and 2.5 mmol L^{-1} potassium ferrocyanide ($K_4Fe(CN)_6{\cdot}3H_2O$).

2.5 Photocatalytic Activity Measurement

In this set of experiments, 0.03 g of pure $CuInS_2$, SnS_2 or $CuInS_2/SnS_2$ nano-heterojunction were added in aqueous 100 mL of methyl orange (MO) solution (10 mg L^{-1}). Before the reaction, the suspension was magnetically stirred for 30 min in the dark to reach adsorption–desorption equilibrium. Then the suspension was irradiated by 300 W xenon lamps with a 400 nm cut off filter under magnetic stirring. Every 10 min intervals, 3 mL aliquots were collected from the suspension and immediately centrifuged, and the concentration of MO was analyzed using a 754 UV–Vis spectrometer at 465 nm.

2.6 Regeneration and Reuse of Spent $CuInS_2/SnS_2$ Nano-heterojunction Photocatalyst

In order to evaluate the stability of pure SnS_2 and 0.5% $CuInS_2/SnS_2$ nano-heterojunction catalyst, the catalytic reaction was performed for five times using the same sample. After each cycle, the catalyst separated through centrifugation and washed with deionized water and ethanol several times, then dried at about 100 °C for 4 h. The recovered photocatalyst was used in the next cycle under the same condition as above.

3 Results and Discussion

3.1 XRD Analysis

As is shown in Fig. 1, the XRD patterns demonstrated the characterization of $CuInS_2$, SnS_2 and $CuInS_2/SnS_2$ composites. It can be observed that the $CuInS_2/SnS_2$ composite XRD pattern is consistent with those of pure SnS_2 (JGPDS No. 023-0677). The main diffraction peaks at about $2\theta = 15.03°$, 28.20°, 32.12°, 49.96° and 52.50° could be indexed to the (001), (100), (101), (110) and (111) crystalline planes of tetragonal phase of SnS_2 respectively. While, observing no typical diffraction peak of $CuInS_2$ in the XRD pattern of $CuInS_2/SnS_2$ composite, it is possibly owe to the low loading content of $CuInS_2$.

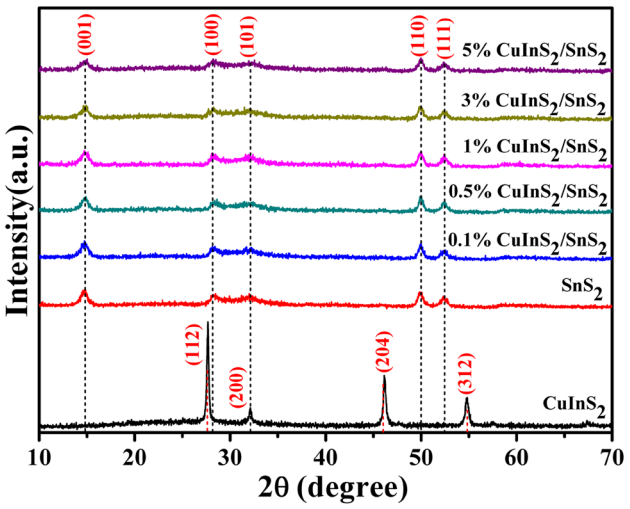

Fig. 1 XRD patterns of pure $CuInS_2$, pure SnS_2 and $CuInS_2/SnS_2$ heterojunctions with different $CuInS_2$ content

3.2 Morphology of Samples

The morphologies of pure SnS_2 and 0.5% $CuInS_2/SnS_2$ nano-heterojunction were characterized by SEM (Fig. 2). Pure SnS_2 was composed of hierarchically porous and flower-like spheres, and these spheres are constructed by many bending 2D sheets which are densely interconnected with each other to form an entangled architecture with a quantity of pores. Non-uniform network-like spheres with an average diameter of 5–8 μm were clearly observed from the low-magnification SEM image of pure SnS_2 (Fig. 2a). The $CuInS_2/SnS_2$ composite shows a rough surface and regular hexahedral shape with a size of 50–70 nm (Fig. 2b).

TEM and HRTEM measurements were performed to further characterize the morphology of 0.5% $CuInS_2/SnS_2$. As shown in Fig. 3a, b, the hexagonal SnS_2 and tetragonal $CuInS_2$ nano-materials were observed. In addition, as can be seen in Fig. 3c, the measured interplanar spacing is 0.32 nm, it maybe belong to the $CuInS_2$ (112) plane or SnS_2 (100) plane. Besides, the SnS_2 (100) and (001) plane interplanar spacing is 0.32 and 0.59 nm, respectively, which is corresponded to the XRD results.

3.3 XPS Analysis

XPS is an important technique for the detection of variations in chemical composition and oxidation state for materials. Figure 4a shows the survey spectrum of 0.5% $CuInS_2/SnS_2$ heterojunction. Cu, In, Sn and S elements are present in the survey spectrum of $CuInS_2/SnS_2$. In addition, the element O (O 1s, 533.14 eV) and C (C 1s, 285 eV) were also obverved in the survey spectrum of $CuInS_2/SnS_2$ due to the organic sulfur precursor and the adventitious hydrocarbon from the XPS instrument itself. Figure 4b–e presented the spectra of Sn 3d, S 2p, Cu 2p and In 3d for $CuInS_2/SnS_2$ heterojunction. In contrast, the Sn $3d_{5/2}$ and Sn $3d_{3/2}$ peaks of SnS_2 nanosheets which appeared at 486.9 and 495.4 eV [25, 26] respectively, are higher than the corresponding binding energy of $CuInS_2/SnS_2$ heterojunction (Fig. 4b). And, two weak peaks which attributed to the Sn–In bonds are found at the Sn 3d core-level of heterojunction nanosheets [27, 28], further indicating the possible bondin configuration of Sn–In on the heterojunction interface. Meanwhile, the S 2p peaks of SnS_2 nanosheets, reflecting to S–Sn bond [25, 26], are also changed to the high binding energy side, when coupling with $CuInS_2$ nanosheets. Compared with pure SnS_2, the Sn 3d states of $CuInS_2/SnS_2$ heterojunction shifted to lower-energy region (Fig. 4b), and the S 2p states of $CuInS_2/SnS_2$ heterojunction shifted to higher-energy region (Fig. 4c), which indicated the migration of electrons from $CuInS_2$ to SnS_2 in the $CuInS_2/SnS_2$ heterojunction [29, 30]. In the $CuInS_2/SnS_2$ heterojunction, the binding energy of Cu $2p_{3/2}$, Cu $2p_{1/2}$, In $3d_{5/2}$ and In $3d_{3/2}$ located at 932.1, 952.1, 445.1 and 452.5 eV, indicating that the oxidation state of copper and indium are +I and +III, respectively (Fig. 4d, e) [31, 32]. According to the XPS analysis, it can be concluded that $CuInS_2/SnS_2$ heterojunctions have been successfully fabricated.

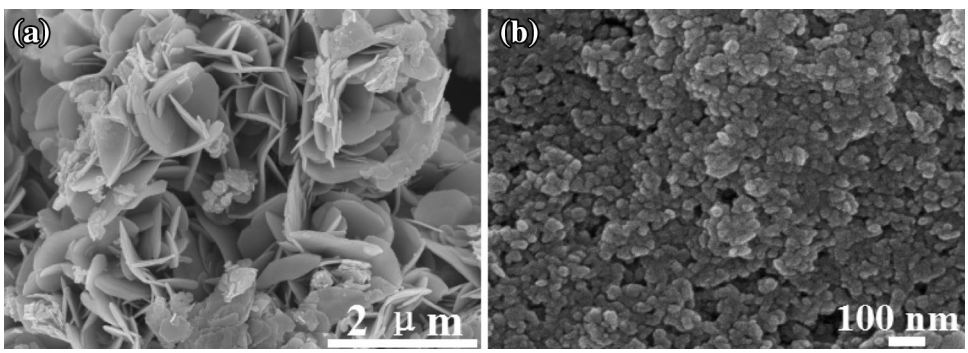

Fig. 2 SEM images of **a** pure SnS_2, **b** 0.5% $CuInS_2/SnS_2$ heterojunctions

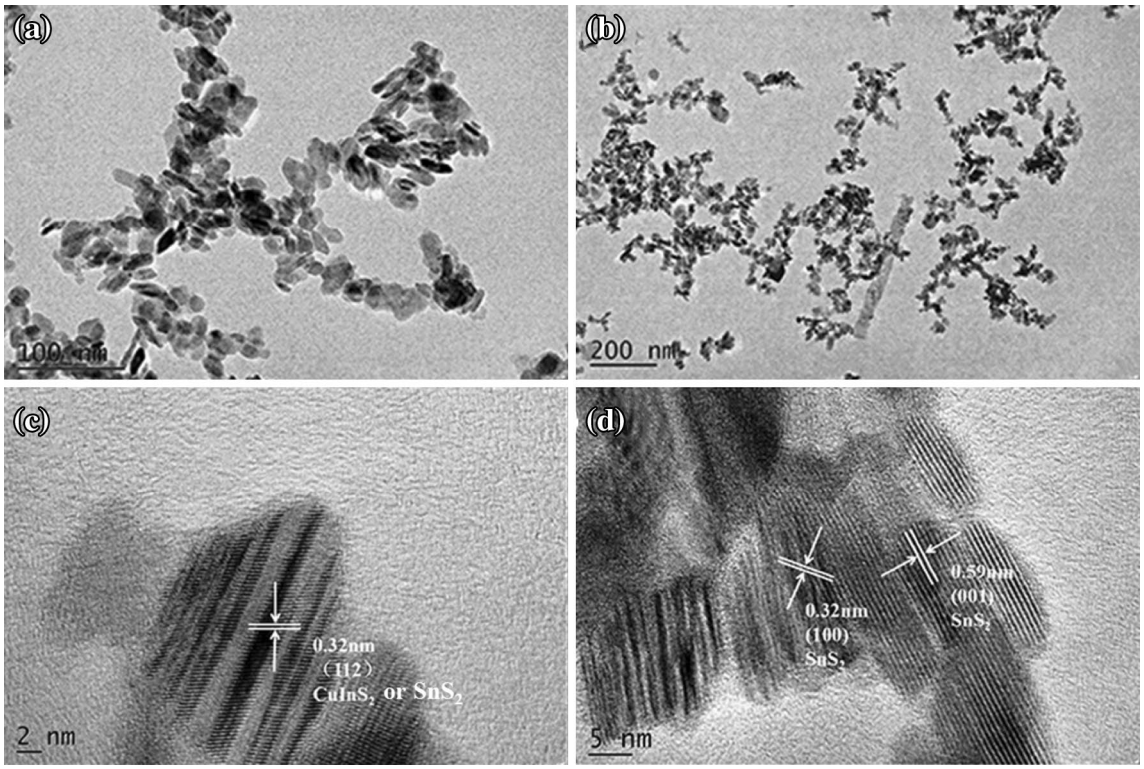

Fig. 3 TEM (**a, b**) and HRTEM (**c, d**) images of 0.5% $CuInS_2/SnS_2$ heterojunctions

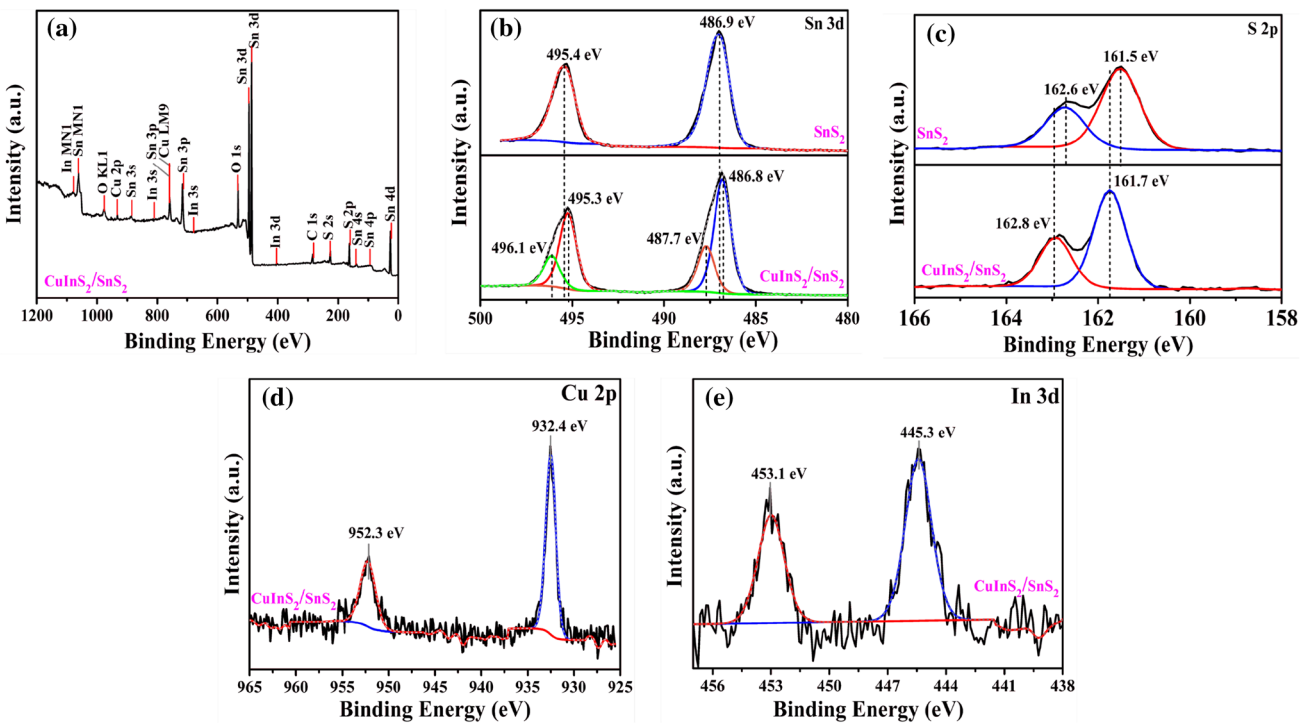

Fig. 4 XPS of **a** survey spectrum, **b** Sn 3d, **c** S 2p, **d** Cu 2p and **e** In 3d of pure SnS_2 and 0.5% $CuInS_2/SnS_2$ heterojunction

3.4 Brunauer–Emmett–Teller Surface Area and Pore Structure

As is depicted in Fig. 5, it was characterized that the N_2 adsorption–desorption isotherms curves of pure SnS_2, $CuInS_2$ and $CuInS_2/SnS_2$ nano-heterojunction with different $CuInS_2$ content. The results demonstrates that it belongs to type IV and H3 hysteresis loop, indicating the existence of mesopores and macro-porous in nano-heterojunction. All the samples showed broad and bimodal pore size distribution with small mesopores (2–4 nm) and larger ones (5–35 nm), further confirming the existence of mesopores. The BET surface area of SnS_2 is 67.9 $m^2\ g^{-1}$. With increasing $CuInS_2$ content from 0.1 to 5%, the specific surface area was greatly increased, the BET surface area of $CuInS_2/SnS_2$ is much higher than that of SnS_2. The main parameters of the samples were listed in Table 1.

Table 1 Physical properties of pure SnS_2, pure $CuInS_2$ and $CuInS_2/SnS_2$ heterojunctions

Samples	S_{BET} ($m^2\ g^{-1}$)	Pore volume ($cm^3\ g^{-1}$)	Average pore size (nm)
SnS_2	67.9	0.17	10.49
$CuInS_2$	32.8	0.18	20.82
0.1% $CuInS_2/SnS_2$	83.7	0.21	9.27
0.5% $CuInS_2/SnS_2$	87.5	0.23	10.70
1% $CuInS_2/SnS_2$	92.7	0.22	9.64
3% $CuInS_2/SnS_2$	96.6	0.26	10.94
5% $CuInS_2/SnS_2$	101.3	0.27	10.92

3.5 UV–Vis Diffuse Reflectance Spectra

As is shown in Fig. 6, the UV–Vis diffuse reflectance spectra of pure $CuInS_2$, pure SnS_2 and $CuInS_2/SnS_2$ heterojunctions with different mass ratio are depicted. Contrasted with pure $CuInS_2$ and pure SnS_2, the $CuInS_2/SnS_2$ heterojunctions absorption intensity was enhanced, with the absorption edge shifting to longer wavelength. Moreover, the band gap energies (E_g) of pure $CuInS_2$, pure SnS_2, and $CuInS_2/SnS_2$ heterojunctions were calculated by Tauc's equation:

$$(\alpha h\nu)^2 = A(h\nu - E_g)^n \tag{1}$$

where α is absorption coefficient, h is planck's constant, ν is light frequency, A is a constant and E_g is band gap energy, and n = 2 for direct-band-gap semiconductor and n = 1/2 for indirect-band-gap semiconductor. The plots of $(\alpha h\nu)^2$ versus $h\nu$ were shown in Fig. 6b, and E_g values were obtained by estimating the intercept of the tangent to the plots. The E_g of pure $CuInS_2$, pure SnS_2, 0.1% $CuInS_2/SnS_2$, 0.5% $CuInS_2/SnS_2$, 1% $CuInS_2/SnS_2$, 3% $CuInS_2/SnS_2$, and 5% $CuInS_2/SnS_2$ heterojunctions were estimated to be about 1.57, 2.1, 1.85, 1.91, 1.81, 1.83 and 1.87 eV, respectively.

3.6 Mott–Schottky Analysis

The flat band potentials (V_{fb}) of $CuInS_2$, SnS_2 and $CuInS_2/SnS_2$ were calculated according to the Mott–Schottky equation (Fig. 7).

$$\frac{1}{C^2} = \frac{2}{A^2 e\varepsilon\varepsilon_0 N_A}\left(E - V_{fb} - \frac{k_B T}{e}\right) \tag{2}$$

where C = interfacial capacitance, A = the electrode surface, E = applied potential, ε = dielectric constant of the semiconductor, ε_0 = permittivity of free space, T = absolute temperature, e = electronic charge, k_B = Boltzmann constant, and N_A = carrier concentration [33]. Hence, V_{fb} values can be obtained when a plot of $1/C^2$ against potential yields a

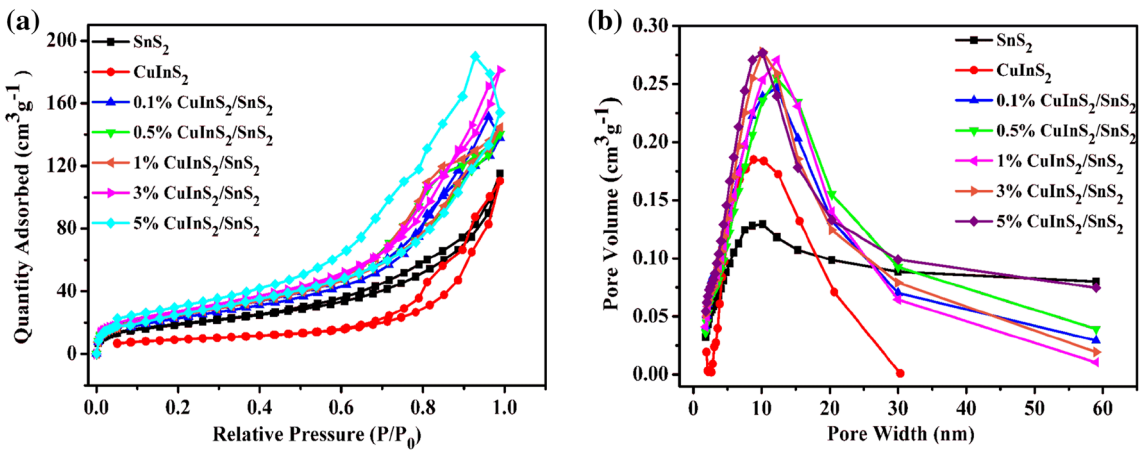

Fig. 5 **a** Nitrogen adsorption–desorption isotherms curves and **b** pore-size distribution curves of pure $CuInS_2$, pure SnS_2 and $CuInS_2/SnS_2$ heterojunctions with different $CuInS_2$ content

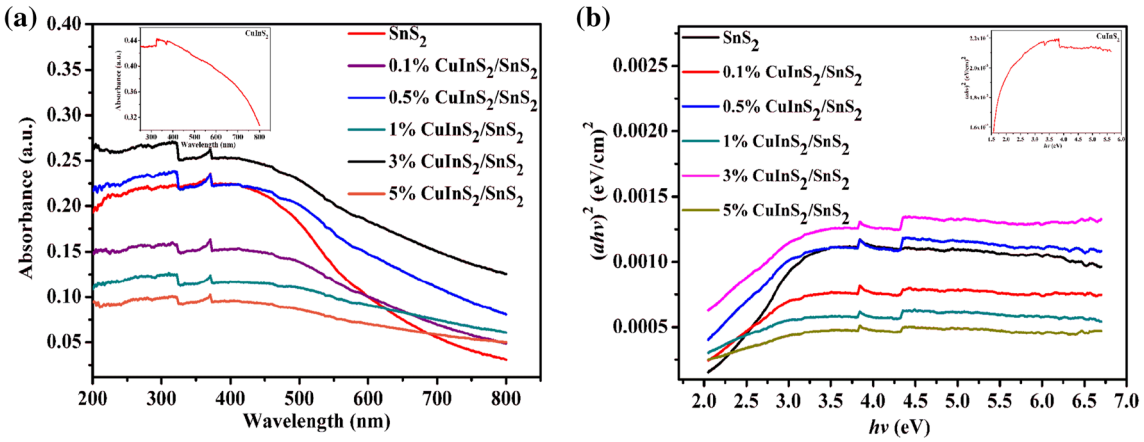

Fig. 6 **a** UV–Vis diffuse reflectance spectra of pure pure $CuInS_2$, pure SnS_2 and $CuInS_2/SnS_2$ heterojunctions with different $CuInS_2$ content and **b** curves of $(\alpha h\nu)^2$ versus $h\nu$

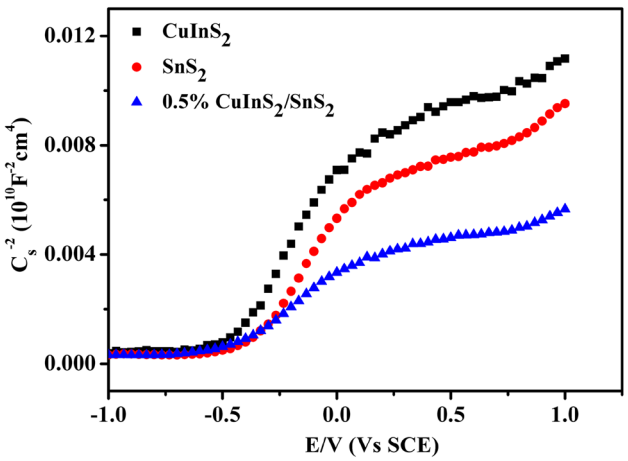

Fig. 7 Mott–Schottky curve of pure $CuInS_2$, pure SnS_2 and 0.5% $CuInS_2/SnS_2$ heterojunction

straight line. The V_{fb} values of $CuInS_2$, SnS_2, 0.5% $CuInS_2/SnS_2$ are −0.538, −0.48, and −0.43 eV versus the saturated calomel electrode (SCE), respectively. The positive shift of the flat band potentials is consistent with their photocatalytic activities. Moreover, the slope of Mott–Schottky lines is positive, indicating $CuInS_2$, SnS_2 and $CuInS_2/SnS_2$ heterojunctions with n-type semiconductor properties.

3.7 Photocurrent Transient and PL Emission Spectra Analysis

The photocurrent transient response test of pure $CuInS_2$, pure SnS_2 and 0.5% $CuInS_2/SnS_2$ heterojunction upon visible-light irradiation was further carried out and the result is shown in Fig. 8. From the Fig. 8a, with light switching on and off, the photocurrent density exhibits a rise and decrease promptly, respectively. Obviously, the photocurrent density of 0.5 wt% $CuInS_2/SnS_2$ heterojunction was higher than that of pure SnS_2 and $CuInS_2$, which suggests that the $CuInS_2/SnS_2$ heterojunction is contribute to rapid separation of photogenerated electrons and holes and agreements with its highest photocatalytic activity. For further detecting the photogenerated electrons and holes recombination, PL emission spectra is usually employed. As Fig. 8b manifested, The PL intensity of 0.5 wt% $CuInS_2/SnS_2$ heterojunction was lower than that of pure SnS_2 and pure $CuInS_2$. The lowest PL intensity of 0.5 wt% $CuInS_2/SnS_2$ indicates the most efficient separation of photogenerated electrons and holes. Both PL and photocurrent results confirmed that the outstanding improvement of charge separation in $CuInS_2/SnS_2$ heterojunction photocatalysts.

3.8 Nyquist Impedance Analysis

To evaluate the probability photogenic electron and holes compound, Nyquist impedance analysis was further carried out (Fig. 9). The alternating current (AC) impedance spectra are obtained by equivalent circuit simulation as shown in Fig. 9b, where C = electric double layer capacitor, Zw = Warburg impedance, Rct = charge transfer resistance and Rs = electrolyte resistance, respectively. The total resistance of pure $CuInS_2$ and SnS_2 is 50 and 296 Ohm, respectively. The total resistance of $CuInS_2/SnS_2$ is only 37 Ohm. It is clear to see that the formation of $CuInS_2/SnS_2$ heterojunction is able to lead to dramatic decrease in the semicycle arc as compared to pure $CuInS_2$ and SnS_2, suggesting a higher charge transfer rate occurred in $CuInS_2/SnS_2$ heterojunction electrode. It is consistent with the PL analysis and photocurrent orders.

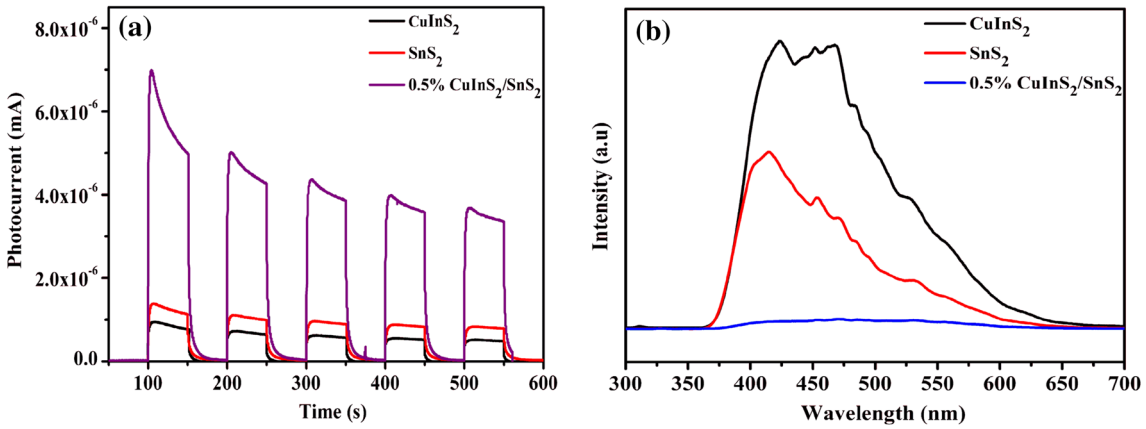

Fig. 8 **a** Photocurrent of pure $CuInS_2$ pure SnS_2 and 0.5% $CuInS_2/SnS_2$ heterojunction under visible-light irradiation, **b** PL spectra of pure $CuInS_2$, SnS_2 and 0.5% $CuInS_2/SnS_2$ heterojunction

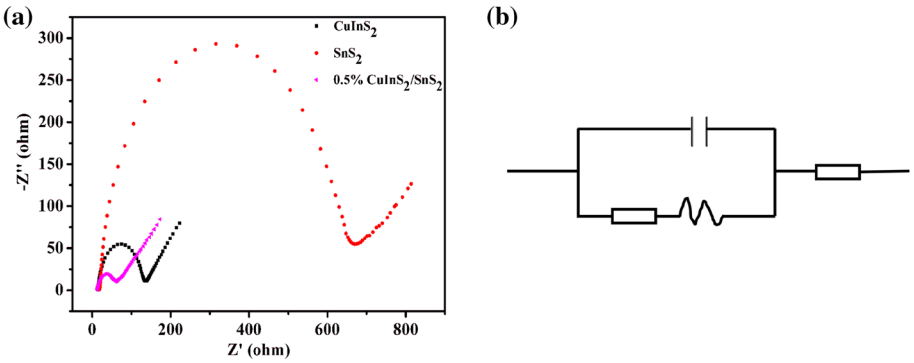

Fig. 9 Electrochemical impedance spectroscopy of the pure $CuInS_2$, SnS_2 and 0.5% $CuInS_2/SnS_2$ heterojunction

3.9 The Evaluation of Photocatalytic Activity

3.9.1 Photocatalytic Performance

The visible-light photocacalytic performance of pure $CuInS_2$, SnS_2 and $CuInS_2/SnS_2$ heterojunction is displayed in Fig. 10. It was clearly to see from Fig. 10 that the photocatalytic activity of $CuInS_2/SnS_2$ heterojunction was higher than that of pure $CuInS_2$. As the amount of $CuInS_2$ increases, the photocatalytic activity increases gradually and then decreases, the order of degradation rate is 0.5 wt% $CuInS_2/SnS_2$ > 0.1 wt% $CuInS_2/SnS_2$ > 1 wt% $CuInS_2/SnS_2$ > 3 wt% $CuInS_2/SnS_2$ > SnS_2 > 5 wt% $CuInS_2/SnS_2$ > $CuInS_2$. The 0.5% $CuInS_2/SnS_2$ exhibits the highest photocatalytic activity, which could be attributed to the optimum $CuInS_2$ content resulting in more efficient generation and transfer of photo-generated electrons and holes at interfaces, but excess $CuInS_2$ can result in the recombination of photo-generated electrons and holes as well as hinder light absorption.

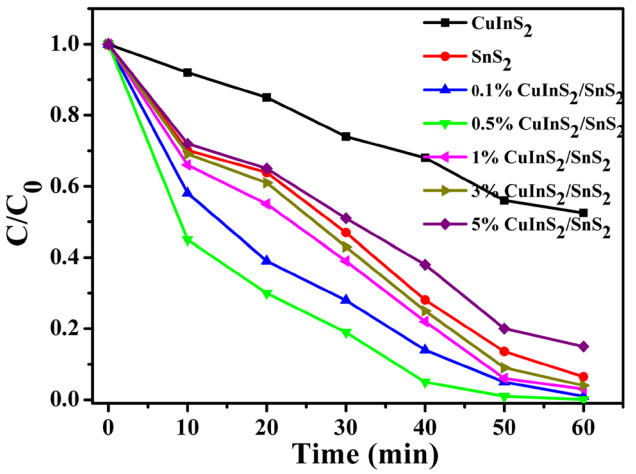

Fig. 10 Photocatalytic activities of pure $CuInS_2$, pure SnS_2 and $CuInS_2/SnS_2$ heterojunctions with different $CuInS_2$ content

3.9.2 Photocatalytic Mechanism

In this part, a tentative photocatalytic reaction mechanism was explored, with IPA ($^{\cdot}OH$ quencher), TEOA (h^+

quencher) and BQ ($^{\cdot}O_2^-$ quencher) beening used and added to the MO solution as scavengers during the MO photodegration process (Fig. 11). As no quenchers added, the MO degradation efficiency reached 99%; while adding TEOA and BQ separately, the degradation efficiency significantly decreased to 23.38% and 15.68%, respectively. Therefore, it can be concluded that the active species ($^{\cdot}O_2^-$ and h^+) have a vital influence on the degradation of MO based on the above results, and the possible photocatalytic mechanism of $CuInS_2/SnS_2$ heterojunction is illustrated in Scheme 1. Under visible-light irradiation, both SnS_2 and $CuInS_2$ can be excited to generate photogenerated electrons (e^-) and holes (h^+). The electrons that excited form $CuInS_2$ conduction band (CB) can inject into CB of SnS_2; besides, the photogenerated holes in VB of SnS_2 have access to transfer easily to the valence band (VB) of $CuInS_2$. Therefore, the separation efficiency of photoinduced charge carriers was remarkably improved by the photosynergistic effect of $CuInS_2/SnS_2$ heterojunction through the photoinduced interfacial charge transfer reducing the recombination of photogenerated e^- and h^+. Since the CB levels of $CuInS_2$ and SnS_2 were more negative than the reduction potential of oxygen E ($O_2/^{\cdot}O_2^-$) (−0.046 V vs. NHE) [34, 35], thus, the photo-generated e^- can react with adsorbed O_2 on the surface of the catalyst to produce $^{\cdot}O_2^-$ radicals. Compared with the potential of $^{\cdot}OH/H_2O$ (2.68 V vs. NHE) and $^{\cdot}OH/OH^-$ (1.99 V vs. NHE) [36], the remained h^+ on the VB of $CuInS_2$ could not react with OH^- or H_2O generating $^{\cdot}OH$ radicals because of the lower VB level of $CuInS_2$ (1.28 V vs. NHE). Subsequently, the highly reactive radical species of $^{\cdot}O_2^-$ and h^+ participated in the photodegration of the MO aqueous solution. The active species trapping experiment results also confirmed that $^{\cdot}O_2^-$ and h^+ were the main reactive species, with $^{\cdot}OH$ beening the less critical one for the degradation of MO.

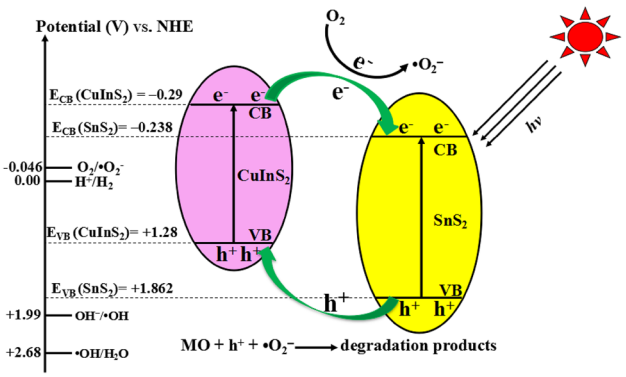

Scheme 1 Schematic illustration for possible photocatalytic mechanism of $CuInS_2/SnS_2$ heterojunction under visible-light irradiation

3.10 Photostability of $CuInS_2/SnS_2$

The reusability is an important property for practical application. Hence, the photostability of 0.5% $CuInS_2/SnS_2$ heterojunction was tested by recycling the photocatalyst for the degradation of MO under visible-light irradiation (Fig. 12). For comparison, the photostability of SnS_2 was also investigated. There is no obviously decline in the photocatalytic degradation efficiency of MO after five degradation–regeneration cycles.

4 Conclusions

$CuInS_2/SnS_2$ heterojunctions were constructed by a facile in situ one step hydrothermal method. The visible-light photocatalytic activity of $CuInS_2/SnS_2$ heterojunctions was influenced by different $CuInS_2$ mass ratio. The optimal

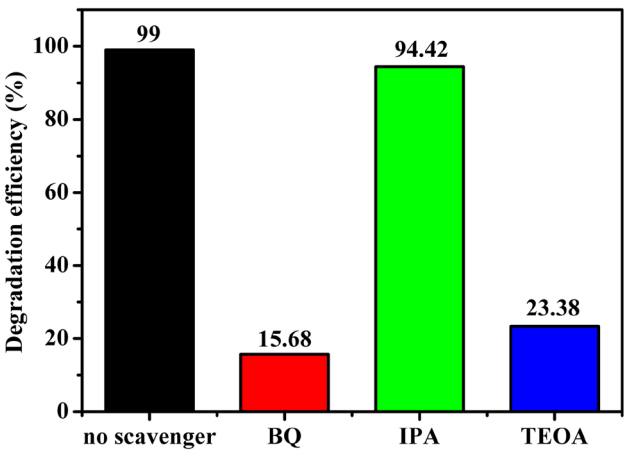

Fig. 11 Effect of different scavengers on the MO photodegradation by 0.5% $CuInS_2/SnS_2$ heterojunction

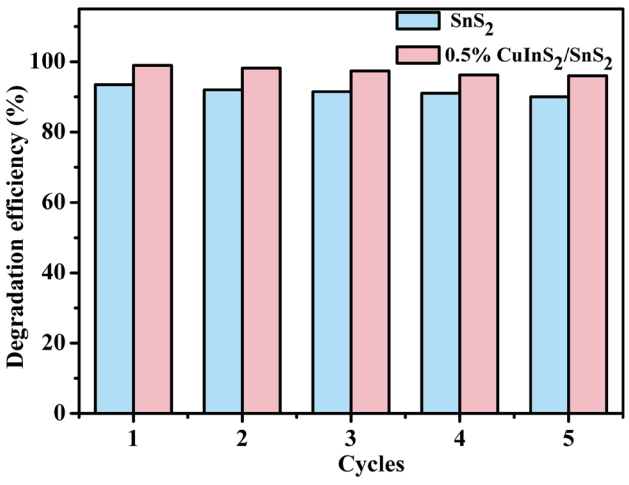

Fig. 12 Reustability of pure SnS_2 and 0.5% $CuInS_2/SnS_2$ heterojunction

0.5% $CuInS_2/SnS_2$ heterojunctions demonstrated the highest visible-light photocatalytic activity, which is almost two times of pure $CuInS_2$. The 0.5% $CuInS_2/SnS_2$ showed the most efficient charge separation and transfer, leading to the highest visible-light photocatalytic activity with 99% degradation efficiency of MO in 60 min. Moreover, $CuInS_2/SnS_2$ heterojunctions show high catalytic stability after five consecutive cycles, which indicating it has a promising prospect in degradation organic pollutant.

Acknowledgements This work supported by the scientific research key project item of Hubei province education office, China (No. D20172904).

References

1. Pulkka S, Martikainen M, Bhatnagar A, Sillanpää M (2014) Electrochemical methods for the removal of anionic contaminants from water-a review. Sep Purif Technol 132:252–271
2. Chong MN, Jin B, Chow CWK, Saint C (2010) Recent developments in photocatalytic water treatment technology: a review. Water Res 44:2997–3027
3. Lachheb H, Puzenat E, Houas A, Ksibi M, Elaloui E, Guillard C, Herrmann JM (2002) Photocatalytic degradation of various types of dyes (Alizarin S, Crocein Orange G, Methyl Red, Congo Red, Methylene Blue) in water by UV-irradiated titania. Appl Catal B 39:75–90
4. Yao Y, Qin J, Chen H, Wei F, Liu X, Wang J, Wang S (2015) Graphitic carbon nitride based nanoheterojunctions: a review, one-pot approach for synthesis of N-doped $TiO_2/ZnFe_2O_4$ hybrid as anefficient photocatalyst for degradation of aqueous organic pollutants. J Hazard Mater 291:28–37
5. Tian J, Hao P, Wei N, Cui H, Liu H (2015) 3D Bi_2MoO_6 nanosheet/TiO_2 nanobelt heterostructure: enhanced photocatalytic activities and photoelectochemistry performance. ACS Catal 5:4530–4536
6. Jin J, Yu J, Guo D, Cui C, Ho W (2015) A hierarchical Z-scheme CdS–WO_3 photocatalyst with enhanced CO_2 reduction activity. Small 11:5262–5271
7. Tian J, Liu RY, Liu Z, Yu CL, Liu MC (2017) Boosting the photocatalytic performance of Ag_2CO_3 crystals in phenol degradation via coupling with trace N-CQDs. Chin J Catal 38:1999–2008
8. Yu CL, Zhou WQ, Zhu LH, Li G, Yang K, Jin RC (2016) Integrating plasmonic Au nanorods with dendritic like α-$Bi_2O_3/Bi_2O_2CO_3$ heterostructures for superior visible-light-driven photocatalysis. Appl Catal B 184:1–11
9. Yu CL, Zhou WQ, Yu JC, Liu H, Wei LF (2014) Design and fabrication of heterojunction photocatalysts for energy conversion and pollutant degradation. Chin J Catal 35:1609–1618
10. Yu CL, Li G, Kumar S, Yang K, Jin RC (2014) Phase transformation synthesis of novel Ag_2O/Ag_2CO_3 heterostructures with high visible light efficiency in photocatalytic degradation of pollutants. Adv Mater 26:892–898
11. Mao LY, Li JJ, Xie YL, Zhong YJ, Hu Y (2014) Controllable growth of SnS_2/SnO_2 heterostructured nanoplates via a hydrothermalassisted self-hydrolysis process and their visiblelight-driven photocatalytic reduction of Cr(VI). RSC Adv 4:29698–29701
12. Mondal C, Ganguly M, Pal J, Roy A, Jana J, Pal T (2014) Morphology controlled synthesis of SnS_2 nanomaterial for promoting photocatalytic reduction of aqueous Cr(VI) under visible light. Langmuir 30:4157–4164
13. Zhang ZY, Shao CL, Li XH, Sun YY, Zhang MY, Mu JB, Zhang P, Guo ZC, Liu YC (2013) Hierarchical assembly of ultrathin hexagonal SnS_2 nanosheets onto electrospun TiO_2 nanofibers: enhanced photocatalytic activity based on photoinduced interfacial charge transfer. Nanoscale 5:606–618
14. Zhang YC, Li J, Xu HY (2012) One-step in situ solvothermal synthesis of SnS_2/TiO_2 nanocomposites with high performance in visible light-driven photocatalytic reduction of aqueous Cr(VI), Appl Catal B 123–124:18–26
15. Khanchandani S, Srivastava PK, Kumar S, Ghosh S, Ganguli AK (2014) Band gap engineering of ZnO using core/shell morphology with environmentally benign Ag_2S sensitizer for efficient light harvesting and enhanced visible-light photocatalysis. Inorg Chem 53:8902–8912
16. Xu QQ, Feng JT, Li LC, Xiao QS, Wang J (2015) Hollow $ZnFe_2O_4/TiO_2$ composites: high-performance and recyclable visible-light photocatalyst. J Alloy Compd 641:110–118
17. Xu Y, Zhang WD (2015) CdS/g-C_3N_4 Hybrids with improved photostability and visible light photocatalytic activity, Eur J Inorg Chem 2015:1744–1751
18. Qiu FZ, Li WJ, Wang FZ, Li HD, Liu XT, Sun JY (2017) In-situ synthesis of novel Z-scheme SnS_2/BiOBr photocatalysts with superior photocatalytic efficiency under visible light. J Colloid Interface Sci 493:1–9
19. Gao XM, Huang GB, Gao HH, Pan C, Wang H, Yan J, Liu Y, Qiu HX, Ma N, Gao JP (2016) Facile fabrication of Bi_2S_3/SnS_2 heterojunction photocatalysts with efficient photocatalytic activity under visible light. J Alloy Compd 674:98–108
20. Zhang ZY, Huang JD, Zhang MY, Yuan Q, Dong B (2015) Ultrathin hexagonal SnS_2 nanosheets coupled with g-C_3N_4 nanosheets as 2D/2D heterojunction photocatalysts toward high photocatalytic activity. Appl Catal B 163:298–305
21. Deng F, Lu XY, Zhao LN, Luo YT, Pei XL, Luo XB, Luo SL (2016) Facile low-temperature co-precipitation method to synthesize hierarchical network-like g-$C_3N_4/SnIn_4S_8$ with superior photocatalytic performance. J Mater Sci 51:6998–7007
22. Yu C, Zhang LL, Tian L, Liu D, Chen FL, Wang C (2014) Synthesis and formation mechanism of $CuInS_2$ nanocrystals with a tunable phase. CrystEngComm 16:9596–9602
23. Siemer K, Klaer J, Luck IK, Bruns J, Klenk R, Bräunig D (2001) Efficient $CuInS_2$ solar cells from a rapid thermal process (RTP). Sol Energy Mater Sol Cells 67:159–166
24. Yuan YJ, Chen DQ, Huang YW, Yu ZT, Zhong JS, Chen TT, Tu WG, Guan ZJ, Cao DP, Zou ZG (2016) MoS_2 nanosheet-modified $CuInS_2$ photocatalyst for visible light-driven hydrogen production from water. ChemSusChem 9:1003–1009
25. Zhang Z, Shao C, Li X, Sun Y, Zhang M, Mu J, Zhang P, Guo Z, Liu Y (2013) Hierarchical assembly of ultrathin hexagonal SnS_2 nanosheets onto electrospun TiO_2 nanofibers: enhanced photocatalytic activity based on photoinduced interfacial charge transfer. Nanoscale 5:606–618
26. Zhang YC, Du ZN, Li KW, Zhang M, Dionysiou DD (2011) High-performance visible-light-driven SnS_2/SnO_2 nanocomposite photocatalyst prepared via in situ hydrothermal oxidation of SnS_2 nanoparticles. ACS Appl Mater Interfaces 3:1528–1537
27. Wu Y, Liu H, Zhang J, Chen F (2009) Enhanced photocatalytic activity of nitrogen-doped titania by deposited with gold. J Phys Chem C 113:14689–14695
28. Zhou B, Dong S, Zhao H, Liu Y, Wu P (2014) Ferromagnetic spin-order in p-type N-doped SnO_2 films prepared by thermal oxidation of SnNx. J Magn Magn Mater 362:14–19
29. Li XH, Xu HY, Zhang XT, Liu YC, Sun JW, Lu YM (2009) Local chemical states and thermal stabilities of nitrogen dopants in ZnO film studied by temperature-dependent X-ray photoelectron spectroscopy. Appl Phys Lett 95:191903(1)–191903(3)

30. Zhang Z, Shao C, Li X, Wang C, Zhang M, Liu Y (2010) Electrospun nanofibers of p-type NiO/n-type ZnO heterojunctions with enhanced photocatalytic activity. ACS Appl Mater Interfaces 2:2915–2923
31. Meng WL, Zhou X, Qiu ZL, Liu CW, Chen JW, J.Yue W, Wang MT, Bi H (2016) Reduced graphene oxide-supported aggregates of $CuInS_2$ quantum dots as an effective hybrid electron acceptor for polymer-based solar cells. Carbon 96:532–540
32. Xu FY, Zhang JJ, Zhu BC, Yu JG, Xu JS (2018) $CuInS_2$ sensitized TiO_2 hybrid nanofibers for improved photocatalytic CO_2 reduction. Appl Catal B 230:194–202
33. Lim J, Murugan P, Lakshminarasimhan N, Kim JY, Lee JS, Lee S, Choi W (2014) Synergic photocatalytic effects of nitrogen and niobium co-doping in TiO_2 for the redox conversion of aquatic pollutants under visible light. J Catal 310:91–99
34. Chai B, Peng TY, Mao J, Li K, Zan L (2012) Graphitic carbon nitride (g-C_3N_4)-Pt-TiO_2 nanocomposite as an efficient photocatalyst for hydrogen production under visible light irradiation. Phys Chem Chem Phys 14:16745–16752
35. Hao RR, Wang GH, Tang H, Sun LL, Xu C, Han DY (2016) Template-free preparation of macro/mesoporous g-C_3N_4/TiO_2 heterojunction photocatalysts with enhanced visible light photocatalytic activity. Appl Catal B 187:47–58
36. He YM, Zhang LH, Teng BT, Fan MH (2015) New application of Z-scheme Ag_3PO_4/g-C_3N_4 composite in converting CO_2 to fuel. Environ Sci Technol 49:649–656

Affiliations

Kai Zhang[1] · Yunhai Zhang[2] · WanJu Zhang[1]

[1] School of Chemistry and Chemical Engineering, Hubei Key Laboratory for Processing and Application of Catalytic Materials, Huanggang Normal University, Huangzhou 438000, China

[2] Key Laboratory for Magnetism and Magnetic Materials, Key Laboratory of Special Function Materials and Structure Design of Ministry of Education, Institute of Material Science and Engineering, Lanzhou University, Lanzhou 730000, China